

Spin transport and spin-caloric effects in (Cr,Zn)Te half-metallic nanostructures: Effect of spin disorder at elevated temperatures from first principles

Roman Kováčik,* Phivos Mavropoulos, and Stefan Blügel
*Peter Grünberg Institut and Institute for Advanced Simulation,
 Forschungszentrum Jülich and JARA, 52425 Jülich, Germany*
 (Dated: March 1, 2024)

An important contribution to the thermoelectric and spin-caloric transport properties in magnetic materials at elevated temperatures is the formation of a spin-disordered state due to local moment fluctuations. This effect has not been largely investigated so far. We focus on various magnetic nanostructures of CrTe in the form of thin layers or nanowires embedded in ZnTe matrix, motivated by the miniaturization of spintronics devices and by recent suggestions that magnetic nanostructures can lead to extraordinary thermoelectric effects due to quantum confinement. The electronic structure of the studied systems is calculated within the multiple scattering screened Korringa-Kohn-Rostoker Green function (KKR-GF) framework. The Monte Carlo method is used to simulate the magnetization in the temperature induced spin disorder. The transport properties are evaluated from the transmission probability obtained using the Baranger-Stone approach within the KKR-GF framework. We find qualitative and quantitative changes in the thermoelectric and spin-caloric coefficients when spin-disorder is included in the calculation. Furthermore, we show that substitutional impurities in CrTe nanowires could considerably enhance the Seebeck coefficient and the thermoelectric figure of merit.

I. INTRODUCTION

The rapidly growing field of spin caloritronics¹ has in recent years given impulse to diverse studies focusing on a coupling between spintronics and thermoelectricity. The strong activity in the field is reflected in numerous conceptual developments, including the spin-Seebeck effect in ferromagnets;² the magneto-Seebeck effect in tunnel junctions;³ molecular junctions⁴ or nanowires;⁵ the spin-orbit-based anisotropy of the Seebeck coefficient;⁶ the thermally induced spin accumulation at half-metal/normal metal interfaces;⁷ the thermal spin-transfer torque;⁸ the spin-based Peltier cooling;^{9–12} the effect of spin disorder on the transport coefficients¹³ and the transverse-transport effects (spin Nernst and anomalous Nernst effect);^{14–16} among other studies.

A strong potential for the design of materials with tailored spin-caloric properties lies in the realm of magnetic nanostructures, which are at the focus of the present paper. The advantages of nanostructured materials and junctions are well known. In the first place, quantum confinement effects are quite pronounced, giving the possibility of electronic structure design by means of geometrical design. Additionally, targeted novel-phase design is possible by out-of-equilibrium growth that can be easily sustained in nanostructures compared to the bulk. Another advantage is that spin transfer is less volatile since the electron spin relaxation length can be larger than the nanostructure diameter. These ideas have been discussed in several works, as follows.

Firstly, the possibility of an enhanced Peltier effect in submicron-sized metallic junctions was suggested.^{9–11} Secondly, a thermoelectric-cooling mechanism was theoretically proposed, based on the adiabatic spin-entropy expansion in a quasi-one-dimensional nano-superstructure (the so called “Konbu” phase) by injecting

a spin current from a ferromagnetic to a paramagnetic metal.¹⁷ The realization of Konbu phases as a result of spinodal nano-decomposition was extensively studied in wide gap diluted magnetic semiconductors.^{18–21} Effective chemical pair interactions between magnetic impurities were found to be attractive and short ranged, suggesting a tendency towards the phase separation.¹⁹ An increase of crossover temperature T_c (either blocking or Curie temperature) results due to the formation of magnetic percolation paths.¹⁸ A new crystal growth method of positioning by seeding and shape controlling was proposed, with 100 Tb/in² density of high- T_c nano-magnets in the semiconductor matrix.²⁰

Regarding the spin-polarized transport, one point that has received little attention is the effect of magnetic moment fluctuations at elevated temperatures, known as *spin disorder*. The well-known effect of spin-disorder-induced resistivity^{22–26} has also its counterparts in the current spin polarization and in the Seebeck and spin-Seebeck effects. While in the bulk of magnetic materials the moment fluctuations are small for temperatures significantly lower than T_c (even up to $\frac{2}{3}T_c$), in nanostructures the surface-to-volume ratio is large and the fluctuations are accordingly stronger. In a previous work,¹³ we reported calculations on spin transport influenced by spin-disorder effects in cobalt nanostructures embedded or not in a copper matrix. In the present study, we shift our focus towards half-metallic materials, where the absence of states in the spin-down channel can act in favor of very pronounced spin-transport effects. Such effects have been studied in the field of spin caloritronics in the case of half-metallic Heusler alloys;^{6,7,27,28} however, no investigation of the spin disorder effect at elevated temperatures has so far been conducted.

In the present report we address this issue, focusing on the effect of temperature-induced spin disorder on the

charge- and spin-current, thermopower, and spin-Seebeck coefficient. Instead of Heusler alloys, we choose CrTe as a model system, as previous studies suggest it can be grown in nanostructured form, within a ZnTe matrix, retaining its half-metallic character (see below). We calculate the transport properties of CrTe thin films and CrTe wires of single-atom cross section (“monoatomic”) embedded in ZnTe. The motivation for choosing monoatomic wires as test systems is that quantum confinement effects should be most pronounced in such structures, which could be fabricated by seed-induced molecular beam epitaxy²⁰ as a limiting case of the Konbu-phase. We work within the Landauer-Büttiker approach, employing the multiple scattering screened Korringa-Kohn-Rostoker Green function (KKR-GF) framework,^{13,29,30} with a realistic treatment of the real-space spin disorder at finite temperatures using a supercell.¹³

This paper is organized as follows. Section II contains a summary of previous works on CrTe. In Sec. III we define the studied model systems, describe the methods used in this work and corresponding computational details. Results are discussed in Sec. IV and the conclusions are given in Sec. V.

II. SUMMARY OF INVESTIGATIONS ON CrTe AND (Cr,Zn)Te NANOSTRUCTURES

A promising material to exhibit the Konbu phase formation is the (Cr,Zn)Te diluted magnetic semiconductor (DMS), composed of a ZnTe matrix with a Cr impurity concentration of about 5%.¹⁹ ZnTe is a semiconductor with a direct band gap of around 2.3 eV,^{31–33} normally crystallizing in the zinc blende (ZB) crystal structure. CrTe in its various phases has been widely studied in the past. It is a ferromagnetic transition metal chalcogenide with $T_c = 334$ K.³⁴ Although its most stable crystal structure is that of the hexagonal NiAs type, it can be grown on various different surfaces adapting to the underlying cubic crystal structure.^{35,36} Theoretical investigations have predicted half-metallicity in the ZB-CrTe structure.³⁷

Electrical and magnetic properties of CrTe were experimentally studied in the bulk form or often in its stable stoichiometric $\text{Cr}_{N-1}\text{Te}_N$ compounds with ordered Cr vacancies. The ferromagnetic phase was found stable under hydrostatic pressure up to 2.5 GPa, where the T_c dropped to 170 K linearly from its ambient pressure value.³⁸ A saturation of the spin disorder contribution to the electrical resistivity ρ in the NiAs structure was observed in the vicinity of T_c as a characteristic kink in $\rho(T)$.^{39–41} Seebeck coefficient measurements were reported for stoichiometric Cr_3Te_4 ⁴² and non-stoichiometric $\text{Cr}_{0.8}\text{Te}$ and $\text{Cr}_{0.9}\text{Te}$ ⁴¹ compounds in the NiAs crystal structure, showing a non-trivial dependence on the Cr/Te ratio.

Room temperature (RT) ferromagnetism ($T_c \approx 300$ K) was reported in $\text{Zn}_{1-x}\text{Cr}_x\text{Te}$ semiconducting thin films

with $x = 0.2$.⁴³ In a more recent study, structural, magnetic and transport properties of the (Cr,Zn)Te compound system were investigated.³⁶ The selected-area electron diffraction method indicated presence of ZB-CrTe coherent with the ZB-ZnTe buffer in both the CrTe thin films and in the CrTe nanocluster precipitates, having a T_c of 247 K and 220 K, respectively. Superparamagnetic behavior was found in the CrTe thin films ($\text{Zn}_{1-x}\text{Cr}_x\text{Te}$ with $x > 0.12$) which further showed metallic conductance ($\rho \approx 10 \mu\Omega \text{ m}$ at RT), in agreement with previously published results.³⁹ The CrTe precipitates ($x = 0.14$) exhibited dirty metallic-like character ($\rho \approx 10^3 \mu\Omega \text{ m}$ at RT) with the $\rho(T)$ spin-disorder kink coinciding with T_c . $\text{Zn}_{1-x}\text{Cr}_x\text{Te}$ samples with $x \leq 0.12$ were found to be highly resistive with $\rho \approx 10^7 \mu\Omega \text{ m}$. Further on, the electronic structure of $\text{Zn}_{1-x}\text{Cr}_x\text{Te}$ DMS was investigated by x-ray magnetic circular dichroism and photoemission spectroscopy. It was concluded that ferromagnetism originates from Cr ions of a single chemical environment with a spatially isotropic electronic configuration.⁴⁴

Numerous ab-initio studies on the bulk properties of CrTe have been reported.^{37,45–49} The stability of the half-metallicity was studied in the case of bulk ZB-CrTe in the experimental lattice parameter of several semiconductors,³⁷ as well as in both Cr and Te terminated (001) surfaces of ZB-CrTe,⁵⁰ non-stoichiometric cubic binary chromium chalcogenides⁵¹ and Cr/Mn chalcogenide interfaces.⁵² A magnetic phase diagram of CrTe based on the Korringa-Kohn-Rostoker ab-initio calculations and Monte Carlo simulations was reported showing good agreement between theory and experiment.⁵³ Recently, the CrTe(001)/ZnTe(001) interface was studied with ab-initio methods showing a coherent change from ferromagnetic half-metal to nonmagnetic insulator.⁵⁴ Further on, the stability of ferromagnetism in quasi-one-dimensional Cr chains embedded in ZnTe was reported.⁵⁵

III. METHOD AND COMPUTATIONAL DETAILS

A. Geometric setup of the model systems

Our model systems are composed of a central region in the zinc blende crystal structure (experimental lattice parameter of ZB-ZnTe $a_{\text{lat}} = 6.1$ Å) sandwiched between half-infinite Ag leads extending in the $\pm z$ -directions (Fig. 1). The central region is formed either by a thin layer (TL) of CrTe or by a monoatomic CrTe wire (W1) embedded in the ZnTe matrix, with Zn/Cr atoms interfacing the leads. The in-plane unit cell of the interface with lattice constant $a_{\text{lat}}/\sqrt{2}$ is shown in Fig. 1(a). The Ag atoms at the interface assume the positions of the Te and vacant sites in the ZB structure. Due to the 5% mismatch between the face-centered cubic Ag lattice parameter (4.1 Å) and $a_{\text{lat}}/\sqrt{2}$, the natural lattice of Ag atoms is compressed in the z direction in order to preserve the

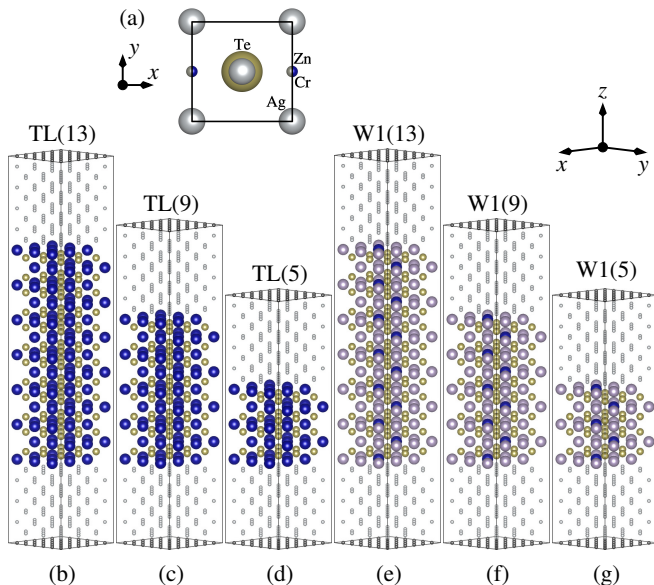


FIG. 1: (Color online) (a) Ag/(Cr,Zn)Te interface unit cell, the layers are ordered along the z direction as Te, Cr/Zn and Ag. CrTe thin layers (TL) (b)-(d) and monoatomic Cr nanowires (W1) embedded in ZnTe matrix (e)-(g) sandwiched between Ag leads (oriented according to the xyz compass). Different elements in (b)-(g) are depicted as large dark spheres (Cr), large bright spheres (Zn), medium size spheres (Te) and small spheres (Ag). The number of Cr layers is 13 [(b),(e)], 9 [(c),(f)], and 5 [(d),(g)]. The structure representations were plotted using VESTA.⁵⁶

Ag unit cell volume. A 3×3 in-plane supercell is used to model the real-space spin disorder in the CrTe thin layers [Figs. 1(b)–1(d)] and as separation between the in-plane periodic images of the nanowires [Figs. 1(e)–1(g)]. The central region thickness of 13, 9 or 5 Cr layers is chosen to examine the influence of a quasi-3D to 2D transition (in TL systems) or a quasi-1D to 0D transition (in W1 systems) on the transport properties.

B. Terminology

A few words on the terminology of later sections are due. We use the term *core region* for the CrTe/ZnTe region between the Ag leads in the structures, i.e., either the CrTe film or the nanowire with the embedding matrix. By *interface* we mean the interface between the Ag leads and the core region. We further indicate by a number in curly brackets the distance of a given atom to the interface in z direction, e.g., Cr{7} is the seventh Cr atom counting from the interface and Ag{1} is the interface Ag atom. Round brackets are used to declare the thickness of the core region, e.g., W1(13) is the system with the 13-atom-long CrTe nanowire.

C. Self-consistent calculations

The electronic structure of the model systems was calculated by the KKR-GF method using the full-potential formalism^{57–60} and the local density approximation⁶¹ to the exchange-correlation energy functional. The angular momentum expansion was truncated at $l_{\max} = 3$. All structural parameters were kept fixed and the supercell potentials were constructed following the procedure described in Section II.B of Ref. [13]. A well-converged density was reached by using an 18×18 k -point mesh for the integration in the unit cell surface Brillouin zone (SBZ) and a smearing electronic temperature of 800 K.⁶²

It is well known that the local density approximation to density-functional theory underestimates the band gap of semiconductors and insulators. This can pose a practical problem in the transport calculations in systems with ZnTe, increasing the tunneling amplitude to unrealistically high values that could play a spurious role in the thin-spacer systems. We circumvent the problem by adjusting the self-consistent atomic potentials of Zn and Te (by rigid positive shift of the Zn potential and rigid negative shift of the Te potential) such that the band gap value corresponds to the experimental one³³ and the Fermi energy is set in its middle.

D. Spin disorder and electron transport

The calculation method used in this study was in detail described in Ref. 13. However, for completeness, the key steps of the procedure are outlined in this section, where also the details specific to the studied systems are given.

The spin disorder model is based on adopting the moment directions at temperature T as they are given by a classical Heisenberg model

$$H = - \sum_{i,j} J_{ij} \mathbf{M}_i \cdot \mathbf{M}_j. \quad (1)$$

Here, \mathbf{M}_i and \mathbf{M}_j are unit vectors pointing in the direction of the magnetic moments at sites i and j , respectively, while J_{ij} are the exchange parameters extracted from the ground-state electronic structure by means of the method of infinitesimal rotations.⁶³ The moment directions are given in a series of sampling configurations (“snapshots”) at thermal equilibrium at T by means of the Monte Carlo (MC) method employing the Metropolis algorithm⁶⁴ and using the Mersenne twister⁶⁵ for the random number generation. The number of MC sampling configurations N_{conf} necessary for a statistical convergence of the transport properties was chosen proportional to the fluctuation amplitude as described in Ref. 13, yielding typical $N_{\text{conf}} \approx 300$ in the vicinity of T_c , where the moment fluctuations are largest.

The spin-up (majority-spin) and spin-down (minority-spin) directions in the electronic structure and transport calculations for each MC snapshot are calculated with

respect to the global magnetization axis of the same MC snapshot and averaged at the end over all snapshots.

We further define the moment-moment correlation function C_N between moments, averaged over all layer pairs having a distance of N layers (distance of $Na_{\text{lat}}/2$ in the z direction). For a given N , let there be N^{pair} of such pairs in the nanostructure; also, let the first of the layers in the pair be indicated by $c = 1, 2, \dots$, with the in-plane coordinates of the atoms indicated by (a, b) ; this places the second layer at $c + N$ with in-plane coordinates (a', b') . The in-plane supercell contains N_{ab} ($N_a \times N_b$) magnetic atoms. Then we define

$$C_N(T) = \frac{1}{N_{ab}} \sum_{a,b} \frac{1}{N^{\text{pair}}} \sum_c \langle \mathbf{M}_{(a,b);c} \cdot \mathbf{M}_{(a',b');c+N} \rangle_T. \quad (2)$$

In the calculation of C_N we include correlations between pairs (a, b) and (a', b') whose distance, when projected onto the xy plane, does not exceed $a_{\text{lat}}/\sqrt{2}$.

In calculating the transmission, we work within the adiabatic approximation,^{66,67} assuming that the electrons do not exchange energy with the magnetic system while traversing the nano-sized junction and that the magnetic moments can be treated as frozen in their magnitude and direction during this short time interval. The same conceptual real-space approach was applied for the spin-disorder resistivity of ferromagnets,^{24,26} but with the difference that in those works only the high temperature limit of the paramagnetic state (complete spin disorder) was considered. The transmission probability matrix through the non-collinear magnetic structure is calculated by the same code that was developed for Ref. 13; it is based on a combination of the Baranger-Stone⁶⁸ Green function approach to the Landauer-Büttiker theory and on the KKR-GF method.^{29,57}

A further approximation is that we accept a rotation of the ground-state magnetic part of the site-dependent potentials in the instantaneous direction prescribed by the MC. This is done without a self-consistent calculation of the non-collinear state, which would result in an increase of computational time by one to two orders of magnitude. We verified that the magnitude of the magnetic moments in the non-collinear state differ very little from their respective values at the ground state. From this we conclude that the intra-atomic exchange interaction is dominant over the inter-atomic interaction for the moment formation, justifying the non-self-consistent approximation.

The basic quantities in (spin)-thermoelectric calculations are the well-known transport coefficients \mathbf{L}_n (here, boldface font implies a 2×2 matrix in spin space). These were evaluated by a numerical integration of the transmission probability $\Gamma(\mathbf{k}_{\parallel}, E)$ ¹³ [which is also a matrix in spin space with elements $\Gamma^{\sigma\sigma'}(\mathbf{k}_{\parallel}, E)$] over the crystal momentum \mathbf{k}_{\parallel} and energy E as

$$\mathbf{L}_n = - \int dE (E - E_F)^n \frac{\partial f_T(E)}{\partial E} \int_{\text{SBZ}} d\mathbf{k}_{\parallel} \Gamma(\mathbf{k}_{\parallel}, E). \quad (3)$$

Here, $f_T(E) = \left[\exp\left(\frac{E - E_F}{k_B T}\right) + 1 \right]^{-1}$ is the Fermi-Dirac distribution function, T is the temperature of the MC simulation, and E_F is the Fermi energy. For each temperature and system, $\Gamma(E) = \int_{\text{SBZ}} d\mathbf{k}_{\parallel} \Gamma(\mathbf{k}_{\parallel}, E)$ was calculated on a mesh of 15 equidistant points in the range $-7k_B T \leq (E - E_F) \leq +7k_B T$, beyond which $(E - E_F)^n \partial f_T / \partial E$ practically vanishes. Tests on denser grids gave insignificant differences. Finally, $\langle \mathbf{L}_n \rangle_T$ is calculated as an average over the non-collinear MC configurations.

The electrical conductance G , electrical resistance R , charge Seebeck coefficient S_C and spin Seebeck coefficient S_S , the thermal conductance K , and the thermoelectric figure of merit ZT are calculated using the well-known formulas

$$G^{\sigma\sigma'}(T) = \frac{e^2}{h} \langle L_0^{\sigma\sigma'} \rangle_T \quad (4)$$

$$G = \sum_{\sigma\sigma'} G^{\sigma\sigma'} \quad (5)$$

$$R = \frac{1}{G} \quad (6)$$

$$S_C = - \frac{\sum_{\sigma\sigma'} \langle L_1^{\sigma\sigma'} \rangle_T}{eT \sum_{\sigma\sigma'} \langle L_0^{\sigma\sigma'} \rangle_T} \quad (7)$$

$$S_S = - \frac{\langle L_1^{\uparrow\uparrow} \rangle_T + \langle L_1^{\downarrow\downarrow} \rangle_T - \langle L_1^{\uparrow\downarrow} \rangle_T - \langle L_1^{\downarrow\uparrow} \rangle_T}{eT \sum_{\sigma\sigma'} \langle L_0^{\sigma\sigma'} \rangle_T} \quad (8)$$

$$K = \frac{\sum_{\sigma\sigma'} \langle L_2^{\sigma\sigma'} \rangle_T - \left(\sum_{\sigma\sigma'} \langle L_1^{\sigma\sigma'} \rangle_T \right)^2}{T \sum_{\sigma\sigma'} \langle L_0^{\sigma\sigma'} \rangle_T} \quad (9)$$

$$ZT = \frac{GT}{K} S_C^2. \quad (10)$$

IV. RESULTS AND DISCUSSION

A. Electronic structure of the collinear magnetic state

Before we proceed to the analysis of the transport properties, we briefly discuss the electronic structure of the model systems before imposing temperature on the magnetic system and non-collinear magnetism. The self-consistent calculations were performed assuming a collinear magnetic ground state. However, a detailed inspection of the exchange coupling parameters (not shown here) already indicates that in the thin layers the interface Cr moments tend to a non-collinear ground state. Monte Carlo simulations indeed show that while the film-interior magnetization, i.e., deeper than in the interface layer, remains practically collinear, moments at the interface tilt away from the film-interior magnetization but not fully reaching the spin-flop state. Their projection to the plane normal to the film-interior magnetization forms a checkerboard pattern. The non-collinearity at low temperatures is accounted for in the conductance calculations (see next Sec. IV B for more details). Wires, on the other hand, show a collinear ground state.

The k_{\parallel} -resolved density of states (DOS) along the X- Γ -M path in the surface Brillouin zone is shown for selected sites and systems in Fig. 2. Each panel in Fig. 2(a) is divided in left/right sub-panels for majority/minority spin channels. The first four panels from left in Fig. 2(a) correspond to the TL(13) system with a 1×1 unit cell cross-section, i.e., the system has one atom per layer in the two-dimensional unit cell in the CrTe part of the slab, as shown in Fig. 1(a). The DOS at the Cr{7} atom, located at the center of the core region, is essentially bulk-like, characterized by the p bands of Te at 2 to 5 eV below E_F , partially occupied majority spin d bands of Cr and the bottom edge of the minority spin Cr d bands just above E_F . Similarly, the DOS of Ag{4} (fourth Ag atomic layer from the interface) already shows bulk-like behavior, with the lower edge of the characteristic s band at 8 eV below E_F crossed by d character bands between 6 and 2.5 eV below E_F and with the DOS at E_F dominated by an sp band. The DOS at the interface Ag{1} and Cr{1} atoms shows well preserved d bands of the corresponding element. Interface states of sp character appearing just above E_F are completely suppressed in the Ag{7} layer (not shown).

The first four panels from left in Fig. 2(b) correspond to the system which is geometrically identical to the previously discussed one but the core region consists of ZnTe instead of CrTe and serves as a matrix for the W1(13) nanowire. The DOS at the Zn{7} atom, located in the center of the slab, is characterized by fully occupied d bands of Zn at 6 eV below E_F and the Te p bands right above them, separated from the Zn s bands by a direct band gap at the Γ point. Note that the ZnTe gap was manipulated to reach the experimental value as described in Sec. III C. The DOS of Ag{4} is very similar to that of Fig. 2(a) and likewise, the sp interface state is quickly suppressed with essentially no trace present in the Ag{7} layer (not shown).

The rightmost panels in Fig. 2(a) and Fig. 2(b) show the DOS of the Cr site in the nanowire and the Zn site farthest from the Cr nanowire (second nearest in-plane neighbor), respectively, in the central layer of the W1(13) system. As can be seen in the Cr{7}-W1(13) panel of Fig. 2(a), the dispersion of Cr d bands is narrowed down while it is widened for the Te p bands due to the strong influence of the ZnTe matrix [compare to the Zn{7}-TL(13) panel in Fig. 2(b)]. As a result, the minority spin band gap is slightly smaller and shifted upwards. The Zn{7}-W1(13) panel in Fig. 2(b) shows that the semiconducting nonmagnetic character of ZnTe DOS is well preserved in the ZnTe matrix surrounding the Cr nanowire.

While the difference between the DOS of the individual TL systems in their central layer is rather small, the same is not true in the case of the nanowires. Figure 2(c) displays the Cr atom DOS of the nanowire central layer in a narrow energy range around E_F , where the dominant contributions to the transport properties are calculated. A characteristic pattern can be recognized for all three systems, with strongly smeared-out features in case of

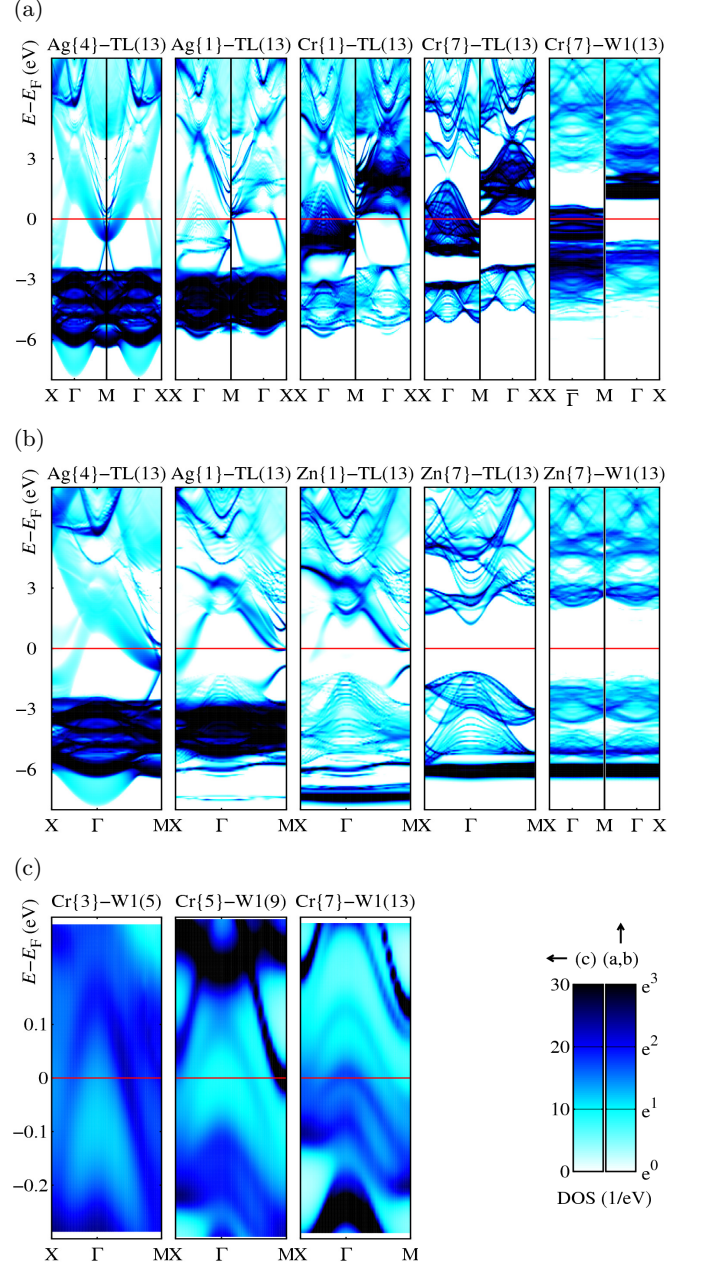


FIG. 2: (Color online) The k -resolved density of states (DOS) along the X- Γ -M path in the surface Brillouin zone. The first four panels in (a) and (b) correspond to the total DOS of selected sites in the Ag/CrTe/Ag (a) and Ag/ZnTe/Ag (b) systems with 1×1 unit cell cross-section and 13 Cr (or Zn) layers. The number in curly brackets in the graph label denotes the distance of the labeled site from the interface. The rightmost panel in (a) and (b) corresponds to the DOS of the Cr site in the nanowire and the Zn site farthest from the Cr nanowire, respectively, in the central layer of the W1(13) system. Panels divided by a vertical line show the majority/minority DOS in their left/right part. (c) k -resolved DOS at the central Cr atom of the W1(5), W1(9) and W1(13) nanowires in a narrow energy range around the Fermi level (indicated by horizontal line at $E = 0$ in all graphs of this figure).

the shortest W1(5) nanowire. In addition, an upward shift of the bands with increasing nanowire length is evident. Although the shift tends to decrease gradually as the nanowires get longer, it could potentially lead to a large difference in the transport properties between the nanowires of different lengths.

B. Spin disorder effect on the transport properties

In the following, we use the terms “spin ordered” and “collinear” as synonyms. We make this clarification because the true ground state at the interface of the TL systems is non-collinear but still spin ordered in a checkerboard pattern (as we discussed in the beginning of Sec. IV A).

Figure 3(a) shows the temperature dependence of the average magnetization and the magnetic susceptibility $\chi(T)$ per system. While the divergence of χ is associated with the critical temperature in bulk systems, a falloff of C_N with temperature [Fig. 3(b)] is a good indicator of the loss of magnetic order in thin layers and nanowires.¹³ Here it is convenient to define a reasonably low threshold below which the C_N associated with the long range magnetic order is considered small and the correlation in a distance of N Cr atoms is practically lost. The choice of the threshold value is necessarily somehow arbitrary; we set it to 0.1 for $C_{N>3}$, shown by a dotted horizontal line in Fig. 3(b), for which the corresponding temperature of the most bulk-like TL(13) system coincides with the susceptibility peak.

The loss of long range order can be also identified as a kink in the resistance-*vs.*-temperature plot [Fig. 3(c)]. Looking first at the TL(13) system, the susceptibility peaks at $T \approx 400$ K. Although the growth rate of $R(T)$ is reduced at this temperature, the resistance keeps increasing. The not very pronounced kink at 400 K can be associated with the decrease of C_3 under 0.1. Further increase of $R(T)$ is consistent with a slow falloff of $C_2(T)$. Essentially identical behavior can be seen in the case of the TL(9) system. For the TL(5) system, the kink position is slightly shifted to a lower temperature and the character of C_4 , i.e., the correlation between Cr moments in the two interface layers, is significantly changed. In the case of nanowires, the susceptibility peak can not be associated with any significant feature driven by the spin disorder. The average magnetization stays sizeable up to high temperatures and no clear sign of a kink in $R(T)$ is present. Although the $C_3 < 0.1$ condition is fulfilled for the W1(5) and W1(9) systems in the examined temperature range, the preservation of a strong short range order (see C_2) masks any possible kink in $R(T)$.

Assuming that the CrTe layer became thicker and more bulk-like, it would be interesting to evaluate the resistivity instead of the resistance (practically excluding interface-resistance effects). The spin disorder contribution to the resistivity can be derived from the slope of the linearly increasing resistance as a function of thickness of

the core region (lead-to-lead distance). We derive it from the resistance values of the systems with 13 and 9 Cr layers at $T = 500$ K (where the spin disorder is almost saturated) as $\rho_{sd} = N_{Cr} a_{lat} (R_{500\text{ K}}^{(13)} - R_{500\text{ K}}^{(9)})/4$. Here, N_{Cr} is the number of Cr atoms in the supercell cross-section (9 for TL and 1 for W1 systems). The calculation results in values of 12 and 5 $\mu\Omega$ m for the CrTe slab and monoatomic wire, respectively. The former value is in reasonable agreement with the experimental estimate of the joint spin disorder and phonon contribution to the resistivity (20 $\mu\Omega$ m) of bulk $\text{Cr}_{0.9}\text{Te}$ in the NiAs structure measured at 400 K,^{41,70} as well as with the more recent measurement of the CrTe thin film resistivity at RT (≈ 10 $\mu\Omega$ m).³⁶

In order to further analyze the transport properties, we present the energy dependent and spin resolved DOS in the core region central layer and the transmission probability Γ , as well as the \mathbf{k}_{\parallel} -resolved Γ , for the thin layers in Fig. 4 and for the nanowires in Fig. 5. The up and down spin projected transmission probabilities are calculated from the individual matrix elements as $\Gamma^{\uparrow} = \Gamma^{\uparrow\uparrow} + (\Gamma^{\uparrow\downarrow} + \Gamma^{\downarrow\uparrow})/2$ and $\Gamma^{\downarrow} = \Gamma^{\downarrow\downarrow} + (\Gamma^{\uparrow\downarrow} + \Gamma^{\downarrow\uparrow})/2$, respectively. All data sets in the graphs as a function of energy are plotted as solid lines in the energy range of $E_F \pm 7k_B T$ in the case of spin disorder, while dotted lines in the energy range $E_F \pm 7k_B \times 500$ K are used for the spin ordered (magnetic collinear) case. Although it is well established that DOS features are not sufficient to determine the character of the transmission probability, we examine first whether such connection could be found in our systems. For brevity, we refer to the majority and minority spin channel as \uparrow and \downarrow (see Sec. IIID for the spin axis convention).

The DOS of all TL systems is very similar, not only at the $T = 0$ K calculations but also at elevated temperatures [Fig. 4(a)]. The DOS^{\uparrow} at 0 K exhibits an asymmetry around E_F which is not reflected in the character of $\Gamma^{\uparrow}(E)$ at 0 K [Fig. 4(b)]. The bottom edge of the Cr d minority spin band that can be seen in the DOS^{\downarrow} at 0 K for $E - E_F > 0.2$ eV manifests itself only very weakly in $\Gamma^{\downarrow}(E)$ [Fig. 4(c)]. The spin disorder leads to almost equal DOS^{\uparrow} and DOS^{\downarrow} above T_c as expected, but the onset of the spin mixing at low temperatures is very slow. The effect of spin disorder on Γ^{\uparrow} has also a slow onset at low T but gradually a clear asymmetry around E_F develops, consistently with the DOS^{\uparrow} . The Γ^{\uparrow} suppression due to the spin disorder is obviously proportional to the thickness of the core region (i.e., the system is in the Ohmic regime at high T).

Very different picture can be seen for Γ^{\downarrow} , which displays an immediate fast onset at low T that then remains almost temperature independent. This effect originates from the Cr atoms at the interface layer favoring the non-collinear ground-state configuration described in Sec. IV A. Since the self-consistent electronic structure was calculated in the collinear state and the spin-ordered calculations refer to this state, they show a suppression of Γ^{\downarrow} by the half-metallic gap.

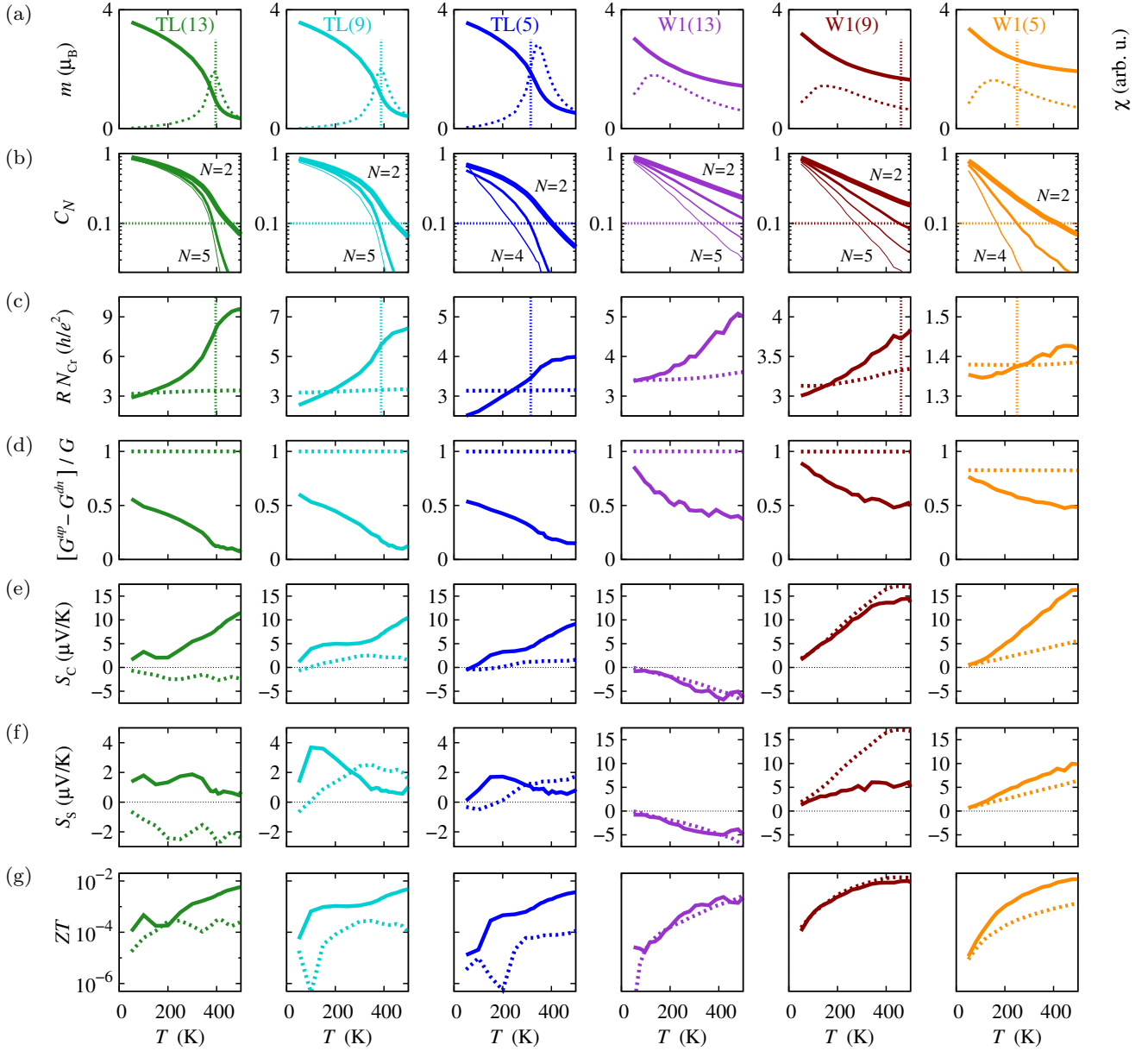


FIG. 3: (Color online) (a) Monte Carlo site averages of the Cr atoms magnetic moment m (solid line) and susceptibility χ (dashed line). (b) Spatial correlation C_N of the magnetic moment orientation between N -th nearest neighbor layers in the z direction. Thick-to-thin line corresponds to second to N -th nearest neighbors, respectively. Vertical dotted line in (a) [and (c)] indicates temperature for which C_3 drops under 0.1 [intersection with dotted line in (b)]. (c) Electrical resistance multiplied by the number of Cr atoms in the supercell cross-section (9 and 1 for TL and W1 systems, respectively). (d) Polarization of the electrical conductance. (e) Charge- and (f) spin-Seebeck coefficient. (g) Thermoelectric figure of merit. In (c)-(g), dashed and solid line corresponds to the spin-ordered and spin-disordered data, respectively.

When accounting for the non-collinear state at the interface at $T \rightarrow 0$ (where the interior of the spacer is half-metallic), spin-flip processes occur, during which an incoming spin-down electron from the lead is flipped at the first interface to spin-up, passes the magnetic spacer and may or may not be flipped back to spin down at the second interface (where again the moments form a non-collinear state). Thus Γ^\downarrow can be non-zero even if the central part of the spacer is perfectly half-metallic.

Overall, this effect leads to an increased conductance (decreased resistance) at low T as can be seen in Figs. 4(d) and 3(c), especially pronounced in the thin quasi-2D TL(5) system. While it may, in general, go unnoticed when looking at the resistance of thicker systems, the effect leaves an almost identical fingerprint in the conductance polarization at low T for all different TL systems irrespective of their thickness [Figs. 3(d) and 4(e)]. Further temperature increase affects the conduc-

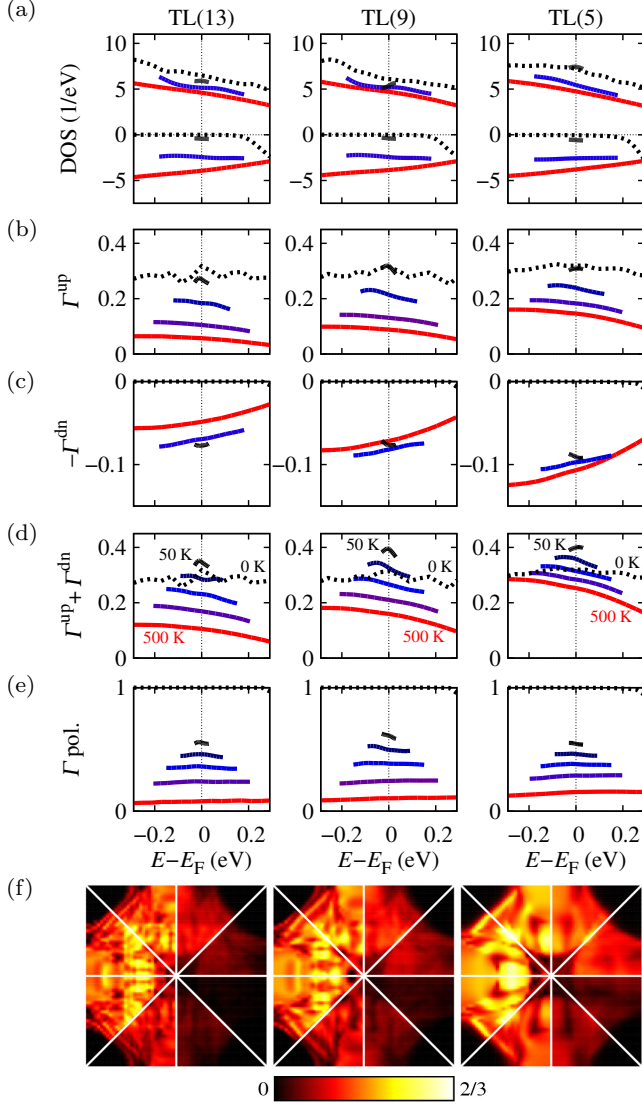


FIG. 4: (Color online) (a) DOS at the Cr atoms in the central layer of the TL systems (positive and negative values correspond to the \uparrow and \downarrow spin, respectively). The transmission probability Γ for (b) \uparrow and (c) \downarrow spin, (d) total transmission probability and (e) its polarization $(\Gamma^{\uparrow} - \Gamma^{\downarrow})/(\Gamma^{\uparrow} + \Gamma^{\downarrow})$. Dotted and solid line in (a)-(e) correspond to the spin ordered and disordered data, respectively, the energy range of spin disordered data corresponds to $\pm 7k_B T$ around E_F , where T is the MC simulation temperature. (f) The transmission probability as a function of k_{\parallel} within the surface Brillouin zone in the systems with 1×1 unit cell cross-section. The irreducible wedges of the SBZ in the upper and lower half of the plots represent $\Gamma^{\uparrow} + \Gamma^{\downarrow}$ and $\Gamma^{\uparrow} - \Gamma^{\downarrow}$, respectively, while from left to right the wedges correspond to the collinear case and the temperatures 100 K, 300 K and 500 K.

tance polarization [Fig. 3(d)] of the TL systems also in a similar way. A weakly pronounced kink at T_c can be seen, above which the polarization is negligible. The transmission probability as a function of k_{\parallel} is shown in Fig. 4(f) only for E_F , since no qualitative differences can be ob-

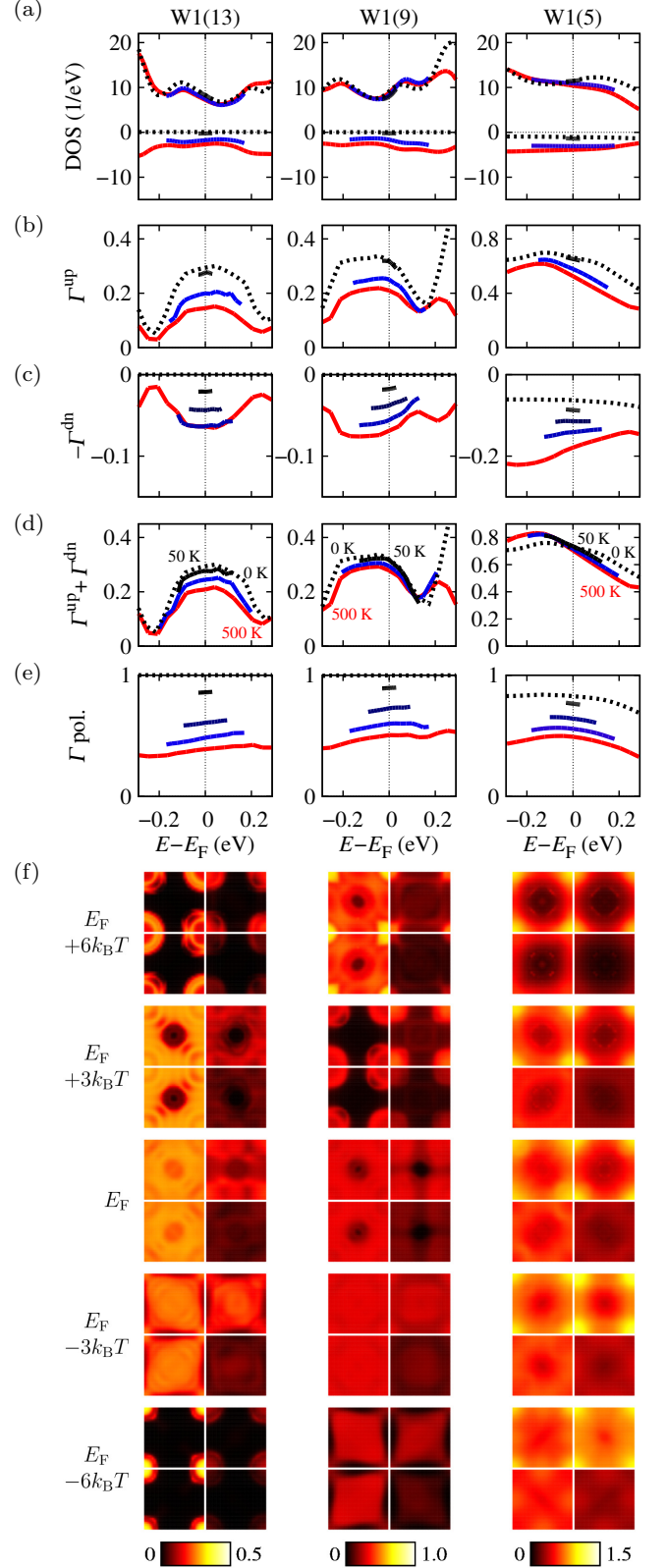


FIG. 5: (Color online) DOS at the central layer Cr atom of the W1 systems. For (a)-(e) plots, the corresponding description in Fig. 4 is valid. (f) The $\Gamma^{\uparrow} + \Gamma^{\downarrow}$ and $\Gamma^{\uparrow} - \Gamma^{\downarrow}$ are shown in the upper and lower half of the plots, respectively, as a function of the energy around E_F and k_{\parallel} within the surface Brillouin zone. The left and right part of the SBZ correspond to the temperature of 0 K and 500 K, respectively.

served in the considered energy range. In this figure, each triangular region corresponds to the irreducible part of the SBZ for different temperatures and for the sum or difference of Γ^\uparrow and Γ^\downarrow , as described in the caption. The region with no conductance around the M point slightly enlarges with increasing T . The fine structure of both Γ and its polarization can be still recognized at $T = 100$ K, while it is almost completely smeared out due to the spin disorder at the room temperature.

The energy dependence of the DOS and Γ is much richer in case of the monoatomic wires. The spin disorder has, in general, a small effect on the DOS [Fig. 5(a)] and even at $T = 500$ K, the DOS^\downarrow is significantly lower than the DOS^\uparrow . The gradual decrease of Γ^\uparrow as a consequence of the spin disorder [Fig. 5(b)] is accompanied by the corresponding increase of Γ^\downarrow [Fig. 5(c)]. The resulting total Γ is therefore only weakly temperature dependent [Fig. 5(d)]. The character of Γ as a function of energy seems to be completely uncorrelated with the DOS, with a possible exception in the peak at $E - E_F = 0.25$ eV for the W1(9) system, which is strongly suppressed in both Γ and DOS. Only the W1(5) system loses half-metallicity at $T = 0$ K, possibly due to a penetration of Ag states throughout the core region.

The conductance polarization [Figs. 3(d) and 5(e)] decreases gradually with temperature similarly to the total magnetization [Fig. 3(a)], remaining sizable at $T = 500$ K. It is worth to note that an energy shift of about 0.15 eV between the characteristic Γ peak of the W1(13) and W1(9) systems is very similar to the energy shift observed in the corresponding structure of \mathbf{k}_\parallel -resolved DOS [Fig. 2(c)]. This shift of about $3k_B T$ can be also identified in the \mathbf{k}_\parallel -resolved Γ . While the W1(13) and W1(9) systems exhibit rather rich fine structure of $\Gamma(\mathbf{k}_\parallel)$, the features of $\Gamma(\mathbf{k}_\parallel)$ are mostly smeared out in the case of the W1(5) system [Fig. 5(f)].

Now we proceed to discuss the charge- and spin-Seebeck coefficient shown in Figs. 3(e) and 3(f), respectively. The charge-Seebeck coefficient S_C of the TL systems in the collinear magnetic case is very low owing to no significant asymmetry in Γ [dotted line in Fig. 4(d)]. The spin disorder has a very similar effect for all TL systems, S_C is positive [negative slope of Γ in Fig. 4(d)] and grows with increasing temperature. The corresponding spin-Seebeck coefficient S_S also becomes consistently positive due to the spin disorder but is almost completely suppressed already at the room temperature. No systematic trend on the nanowire length can be observed for the Seebeck coefficients given the strongly changing character of Γ among the nanowires. Also, while the spin disorder increases both S_C and S_S in the case of W1(5), it induces their decrease for the W1(9) or has just a small effect in the case of W1(13). In Fig. 3(g), we show the resulting figure of merit (ZT). Clearly, its value in all cases is still too low for practical applications, however, the role of spin disorder in its enhancement [except the W1(9) and W1(13) systems] is noteworthy.

C. Substitutional impurity effect on the transport properties of W1(13) nanowire

The strong modulation of $\Gamma(E)$ in the case of the nanowires motivated us to further investigate the effect of a substitutional impurity, as a source of extra scattering, on the transport properties of the nanowire. We chose the W1(13) nanowire as a representative system. The main criterion was the robustness of the Seebeck coefficients of W1(13) with respect to the spin disorder. Furthermore, an energy shift or a shape modulation of the $\Gamma(E)$ peak around E_F could lead to a large enhancement of the Seebeck coefficients as a result of an arising asymmetry. In the W1(13) nanowire, the Cr atom in the wire center was substituted by an element of the fourth period, systematically from potassium to germanium. The electronic structure of each nanowire with the substitutional impurity was calculated self-consistently using the impurity Green function method.^{57,69} Due to the already mentioned Seebeck coefficient robustness with respect to the spin disorder, we first calculated the transport properties for the spin ordered case with a temperature of 470 K entering via the Fermi smearing, the main results of which are summarized in Fig. 6.

A sizable magnetic moment at the impurity site was stabilized for all elements from Ti to Ni [Fig. 6(a)]. While the magnetic moments of Ti and V impurities were aligned in parallel with the overall nanowire magnetization, the anti-parallel alignment was energetically much more favorable for the Mn, Fe, Co and Ni impurities. The resulting majority spin d character occupation of the Mn–Ni sequence is therefore qualitatively similar to the Sc–Cr one. The \mathbf{k}_\parallel -resolved transmission probability is shown in Fig. 6(b) at several energy values around E_F . The character of $\Gamma(\mathbf{k}_\parallel)$ does not only look remarkably alike for the wires with the impurity d shell being essentially empty (K and Ca) or fully occupied (Ga and Ge) but also for the pairs of the transition metal impurities with a similar majority spin d character occupation (with a possible energy shift of the prominent features); namely, Sc is alike to Mn, Ti to Fe, V to Co, Cr (no impurity) to Ni. The \mathbf{k}_\parallel -integrated transmission probability $\Gamma(E)$ around E_F depicted in Fig. 6(c) indeed shows that certain impurities lead to a significant asymmetry of Γ at E_F . Apart from the Ni impurity, which causes a shape preserving energy shift of Γ [compared to the original W1(13) wire], all other impurities lead to a strong Γ modulation. The transport coefficient L_1 as a measure of the Γ asymmetry around E_F is strongly enhanced in case of Sc, Ti and Ni impurities while the L_0 coefficient is generally reduced by all impurities except Ni [Fig. 6(d)]. The Sc and Ti impurities thus lead to an overall enhancement of S_C by an order of magnitude in comparison with the W1(13) nanowire [Fig. 6(e)] and two orders of magnitude increase of ZT , reaching values of about 0.2.

The spin disorder influence on the transport properties was examined in the case of Sc and Ti impurities at room (290 K) and elevated (470 K) temperatures, with

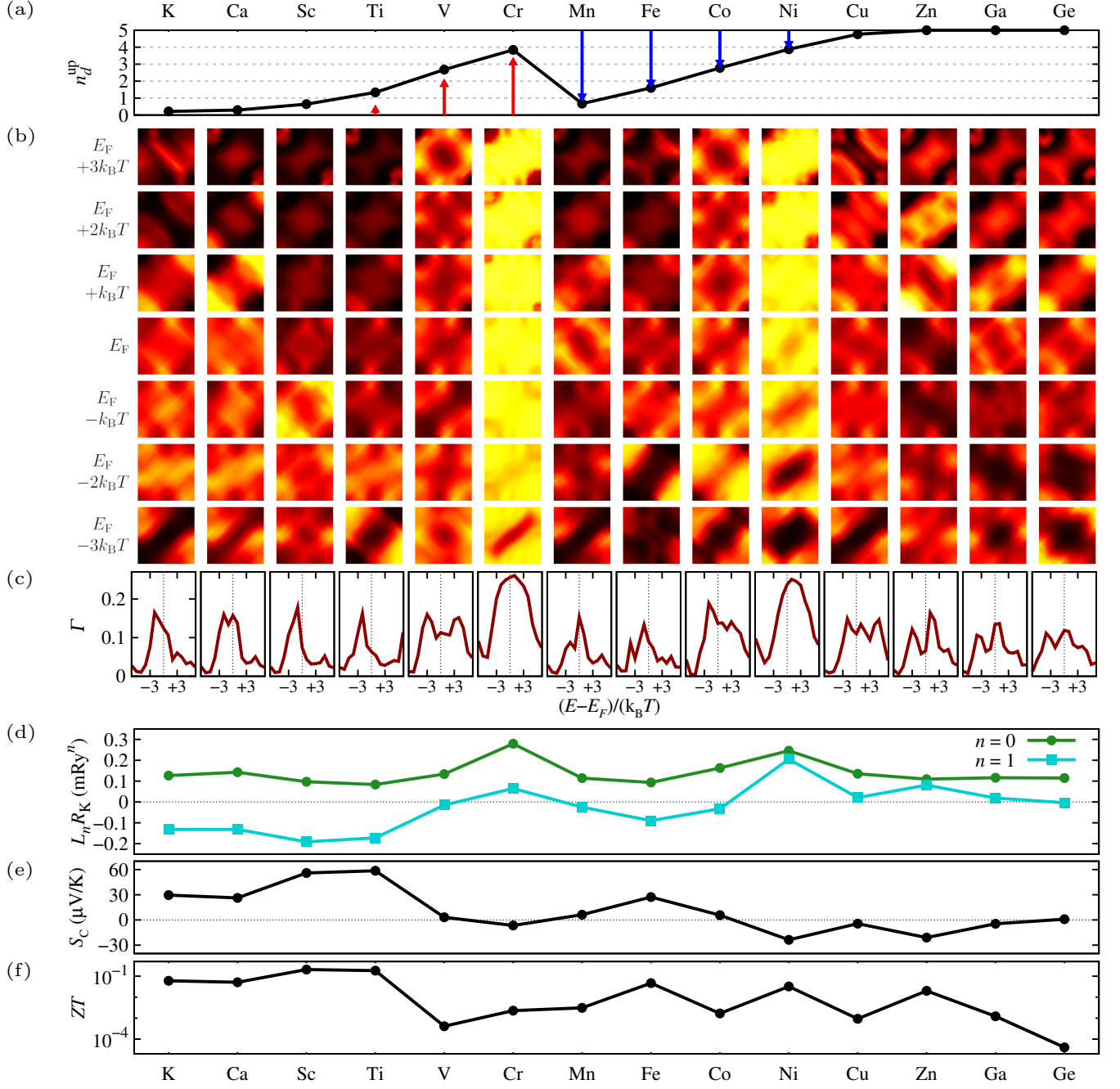


FIG. 6: (Color online) Properties of the W1(13) nanowire with the substitutional impurity in its central layer. (a) Majority spin d orbitals occupation of the impurity site (solid line). Magnetic moment $m(\mu_B)$ of the impurity site (if $m > 0.4 \mu_B$) is represented by a vertical arrow, pointing up/down in case of parallel/antiparallel orientation with the nanowire magnetization. (b) The transmission probability as a function of the energy around E_F and $\mathbf{k}_{||}$ within a section of the surface Brillouin zone (double the irreducible part) defined by Γ (bottom left and top right corner) and M (bottom right and top left corner) high symmetry points, with X point in the center. The gradient color code [equivalent to Figs. 4(f) and 5(f)] corresponds to a linear range of Γ between 0 and 0.37. (c) The $\mathbf{k}_{||}$ -integrated transmission probability as a function of the energy around E_F . (d) The transport coefficients L_0 and L_1 ($R_K = h/e^2$ is the von Klitzing constant). (e) Charge Seebeck coefficient. (f) Thermoelectric figure of merit.

TABLE I: Charge and spin Seebeck coefficients (in $\mu\text{V/K}$) and figure of merit for the W1(13) nanowire with selected substitutional impurities (Sc and Ti). Note that in the spin ordered case, $S_C \approx S_S$ due to negligible $L_n^{\downarrow\downarrow}$, $L_n^{\uparrow\downarrow}$ and $L_n^{\downarrow\uparrow}$ terms in comparison to $L_n^{\uparrow\uparrow}$ for both $n = 0$ and $n = 1$.

impurity	spin order		spin disorder		
	$S_C \approx S_S$	ZT	S_C	S_S	ZT
Sc (290 K)	71	0.27	80	38	0.35
Sc (470 K)	56	0.21	58	25	0.19
Ti (290 K)	47	0.09	58	26	0.12
Ti (470 K)	59	0.18	64	28	0.18

results summarized in Table I. While the $I(E)$ shape is affected only weakly by the spin disorder, the slightly suppressed conductance leads to a further enhancement of the charge Seebeck coefficient. For the Sc impurity, an additional increase at room temperature leads to an S_C of 80 $\mu\text{V/K}$ and a corresponding ZT of 0.35. The spin Seebeck coefficient is reduced to about 45% of the respective S_C value due to the spin disorder, remaining sizable even at elevated temperatures.

V. SUMMARY AND CONCLUSIONS

We have modeled the electron and spin transport properties through CrTe nanostructures (thin layers and monoatomic wires) at elevated temperatures. We focused on the effects of spin disorder, i.e., on the effects of the fluctuating magnetic moments at $T > 0$.

Our calculations show the importance of these effects, both quantitatively and qualitatively. Examining the resistance, current polarization, charge-Seebeck and spin-Seebeck coefficients in a number of structures and temperatures, we find that they depend on system dimensionality (thin layer vs. nanowire), system size (film thickness or wire length) and temperature. Simplifying the calculation by accounting for the electronic temperature (i.e., the Fermi smearing) alone is in many cases not even qualitatively adequate for a description of the transport coefficients; but there are notable exceptions, e.g. in the Seebeck coefficients and ZT of the longer (13-atom) nanowire. Unfortunately, nothing indicates the validity of this simplified and computationally less expensive approach beforehand; it can be verified only *a posteriori*, after the full calculation with spin disorder.

A few general observations can be made about our results. In the thin films, the crossover temperature T_c (at the magnetic susceptibility peak, signaling the strongest magnetic fluctuations) coincides with a change of slope in the resistance-*vs.*-temperature curve, as is known from bulk systems. However, this is not the case in the nanowires, where also the susceptibility peak is less pronounced and the magnetization drop is much smoother. The difference stems possibly from the fact that the fluctuations at T_c in the wires are long-ranged

(due to their lower dimensionality) compared to the films, causing a smoother gradient of magnetization (e.g., infinitely long wires show long-range critical fluctuations at $T_c = 0$). As T grows beyond T_c , the fluctuations in wires become gradually short-ranged, increasing the resistance. In films, T_c is at a point where the fluctuations are already short-ranged (as can be seen from the correlation functions), so that an increase of T does not produce proportionally more scattering; thus the kink is created.

A second observation is that, although the current spin polarization seems to consistently drop with increasing spin disorder, this is not always the case for the spin Seebeck coefficient, especially for the nanowires. At the same time, the current spin polarization of the nanowires is not fully suppressed even at high temperatures. The reason again lies in the long-ranged correlations in the nanowires. The magnetization of a short nanowire behaves to an extent as a macro-spin, i.e., a superparamagnetic entity, so that the fluctuations play a smaller role. Obviously, at very high temperatures or for very long nanowires the transmission as a function of energy must become spin-independent, suppressing the spin-Seebeck coefficient. However, as presented in this study, this is not the case at moderate temperatures or short lengths.

A third observation is that ZT may increase by orders of magnitude either by the effect of spin disorder or if an impurity is placed in the middle of the nanowire. The effect of a substitutional impurity strongly depends on its type, with Sc and Ti being the best candidates through the 3d series for an increased ZT .

Finally, our results contribute to the question on the usefulness of half-metallic ferromagnets in order to achieve spin polarized electron transport. We see from the thin-film calculations that if the interface of a half-metallic magnet to the leads develops a non-collinear magnetic phase, then the current spin polarization drops drastically: under these conditions, the half metallic character in the interior does not improve the current spin polarization compared to the values of a regular ferromagnet. Additionally, non-collinear states at $T > 0$ due to local-moment fluctuations, further reduce the current spin polarization. We also verify the (expected) result that even in the absence of fluctuations, half-metallicity does not imply a strong spin-Seebeck effect, since the same spin channel can contribute positively or negatively to the spin-Seebeck coefficient.

Acknowledgments

We are indebted to Daniel Wortmann, Voicu Popescu and Carmen E. Quiroga for enlightening discussions. Support from the Deutsche Forschungsgemeinschaft (SPP 1538 “Spin Caloric Transport”) is gratefully acknowledged. Computational resources were provided by the JARA-HPC from the RWTH Aachen University under project jara0051.

-
- * Electronic address: r.kovacik@fz-juelich.de
- ¹ G. E. W. Bauer, E. Saitoh, and B. J. van Wees, *Nature Mater.* **11**, 391 (2012).
 - ² K. Uchida, S. Takahashi, K. Harii, J. Ieda, W. Koshibae, K. Ando, S. Maekawa, and E. Saitoh, *Nature* **455**, 778 (2008).
 - ³ M. Walter, J. Walowski, V. Zbarsky, M. Münzenberg, M. Schäfers, D. Ebke, G. Reiss, A. Thomas, P. Peretzki, M. Seibt, et al., *Nature Mater.* **10**, 742 (2011).
 - ⁴ V. V. Maslyuk, S. Achilles, L. Sandratskii, M. Brandbyge, and I. Mertig, *Phys. Rev. B* **88**, 081403 (2013).
 - ⁵ T. Böhnert, V. Vega, A.-K. Michel, V. M. Prida, and K. Nielsch, *Appl. Phys. Lett.* **103**, 092407 (2013).
 - ⁶ V. Popescu and P. Kratzer, *Phys. Rev. B* **88**, 104425 (2013).
 - ⁷ B. Geisler, P. Kratzer, and V. Popescu, *Phys. Rev. B* **89**, 184422 (2014).
 - ⁸ J. C. Leutenantsmeyer, M. Walter, V. Zbarsky, M. Münzenberg, R. Gareev, K. Rott, A. Thomas, G. Reiss, P. Peretzki, H. Schuhmann, et al., *SPIN* **03**, 1350002 (2013).
 - ⁹ A. Fukushima, K. Yagami, A. A. Tulapurkar, Y. Suzuki, H. Kubota, A. Yamamoto, and S. Yuasa, *Jpn. J. Appl. Phys.* **44**, L12 (2005).
 - ¹⁰ A. Sugihara, M. Kodzuka, K. Yakushiji, H. Kubota, S. Yuasa, A. Yamamoto, K. Ando, K. Takanashi, T. Ohkubo, K. Hono, et al., *Appl. Phys. Express* **3**, 065204 (2010).
 - ¹¹ N. D. Vu, K. Sato, and H. Katayama-Yoshida, *Appl. Phys. Express* **4**, 015203 (2011).
 - ¹² B. Scharf, A. Matos-Abiad, I. Žutić, and J. Fabian, *Phys. Rev. B* **85**, 085208 (2012).
 - ¹³ R. Kováčik, P. Mavropoulos, D. Wortmann, and S. Blügel, *Phys. Rev. B* **89**, 134417 (2014).
 - ¹⁴ K. Tauber, M. Gradhand, D. V. Fedorov, and I. Mertig, *Phys. Rev. Lett.* **109**, 026601 (2012).
 - ¹⁵ S. Wimmer, D. Ködderitzsch, K. Chadova, and H. Ebert, *Phys. Rev. B* **88**, 201108 (2013).
 - ¹⁶ J. Weischenberg, F. Freimuth, S. Blügel, and Y. Mokrousov, *Phys. Rev. B* **87**, 060406 (2013).
 - ¹⁷ H. Katayama-Yoshida, T. Fukushima, V. A. Dinh, and K. Sato, *Jpn. J. Appl. Phys.* **46**, L777 (2007).
 - ¹⁸ K. Sato, H. Katayama-Yoshida, and P. H. Dederichs, *Jpn. J. Appl. Phys.* **44**, L948 (2005).
 - ¹⁹ T. Fukushima, K. Sato, H. Katayama-Yoshida, and P. H. Dederichs, *Jpn. J. Appl. Phys.* **45**, L416 (2006).
 - ²⁰ H. Katayama-Yoshida, K. Sato, T. Fukushima, M. Toyoda, H. Kizaki, V. A. Dinh, and P. H. Dederichs, *J. Magn. Magn. Mater.* **310**, 2070 (2007).
 - ²¹ K. Sato, T. Fukushima, and H. Katayama-Yoshida, *Jpn. J. Appl. Phys.* **46**, L682 (2007).
 - ²² S. Arajs and R. V. Colvin, *Phys. Status Solidi* **6**, 797 (1964).
 - ²³ W. Kierspe, R. Kohlhaas, and H. Gonska, *Z. Angew. Phys.* **24**, 28 (1967).
 - ²⁴ A. L. Wysocki, R. F. Sabirianov, M. van Schilfgaarde, and K. D. Belashchenko, *Phys. Rev. B* **80**, 224423 (2009).
 - ²⁵ Á. Buruzs, L. Szunyogh, and P. Weinberger, *Philos. Mag.* **88**, 2615 (2008).
 - ²⁶ J. K. Glasbrenner, K. D. Belashchenko, J. Kudrnovský, V. Drchal, S. Khmelevskiy, and I. Turek, *Phys. Rev. B* **85**, 214405 (2012).
 - ²⁷ J. Barth, G. H. Fecher, B. Balke, S. Ouardi, T. Graf, C. Felser, A. Shkabko, A. Weidenkaff, P. Klaer, H. J. Elmers, et al., *Phys. Rev. B* **81**, 064404 (2010).
 - ²⁸ D. Comtesse, B. Geisler, P. Entel, P. Kratzer, and L. Szunyogh, *Phys. Rev. B* **89**, 094410 (2014).
 - ²⁹ P. Mavropoulos, N. Papanikolaou, and P. H. Dederichs, *Phys. Rev. B* **69**, 125104 (2004).
 - ³⁰ B. Y. Yavorsky and I. Mertig, *Phys. Rev. B* **74**, 174402 (2006).
 - ³¹ S. Larach, R. E. Shrader, and C. F. Stocker, *Phys. Rev.* **108**, 587 (1957).
 - ³² M. Cardona and D. L. Greenaway, *Phys. Rev.* **131**, 98 (1963).
 - ³³ H. Venghaus, *J. Phys. C: Solid State* **17**, 6229 (1984).
 - ³⁴ T. Hirone and S. Chiba, *J. Phys. Soc. Jpn.* **15**, 1991 (1960).
 - ³⁵ A. Goswami and P. S. Nikam, *Thin Solid Films* **11**, 353 (1972).
 - ³⁶ M. G. Sreenivasan, K. L. Teo, X. Z. Cheng, M. B. A. Jalil, T. Liew, T. C. Chong, A. Y. Du, T. K. Chan, and T. Osipowicz, *J. Appl. Phys.* **102**, 053702 (2007).
 - ³⁷ I. Galanakis and P. Mavropoulos, *Phys. Rev. B* **67**, 104417 (2003).
 - ³⁸ B. Lambert-Andron, N. P. Grazhdankina, and C. Vettier, *J. Physique Lett.* **39**, 43 (1978).
 - ³⁹ N. P. Grazhdankina, L. G. Gaidukov, K. P. Rodionov, M. I. Oleinik, and V. A. Shchipanov, *J. Exp. Theor. Phys.* **13**, 297 (1961).
 - ⁴⁰ M. Nogami, *Jpn. J. Appl. Phys.* **5**, 134 (1966).
 - ⁴¹ J. Dijkstra, H. H. Weitering, C. F. van Bruggen, C. Haas, and R. A. de Groot, *J. Phys.: Condens. Matter* **1**, 9141 (1989).
 - ⁴² G. Peix, D. Babot, and M. Chevreton, *J. Solid State Chem.* **36**, 161 (1981).
 - ⁴³ H. Saito, V. Zayets, S. Yamagata, and K. Ando, *Phys. Rev. Lett.* **90**, 207202 (2003).
 - ⁴⁴ M. Kobayashi, Y. Ishida, J. I. Hwang, G. S. Song, A. Fujimori, C. S. Yang, L. Lee, H.-J. Lin, D. J. Huang, C. T. Chen, et al., *New J. Phys.* **10**, 055011 (2008).
 - ⁴⁵ W.-H. Xie, Y.-Q. Xu, B.-G. Liu, and D. G. Pettifor, *Phys. Rev. Lett.* **91**, 037204 (2003).
 - ⁴⁶ P. Mavropoulos and I. Galanakis, *J. Phys.: Condens. Matter* **19**, 315221 (2007).
 - ⁴⁷ Y. Liu, S. K. Bose, and J. Kudrnovský, *Phys. Rev. B* **82**, 094435 (2010).
 - ⁴⁸ L. Vadkhiya, A. Dashora, M. K. Bhayani, A. R. Jani, and B. L. Ahuja, *J. Magn. Magn. Mater.* **322**, 2857 (2010).
 - ⁴⁹ S.-D. Guo and B.-G. Liu, *Europhys. Lett.* **93**, 47006 (2011).
 - ⁵⁰ W. S. Yun and S. C. Hong, *J. Korean Phys. Soc.* **53**, 384 (2008).
 - ⁵¹ S.-D. Guo and B.-G. Liu, *Europhys. Lett.* **88**, 67007 (2009).
 - ⁵² K. Nakamura, T. Akiyama, T. Ito, and A. J. Freeman, *J. Appl. Phys.* **103**, 07C901 (2008).
 - ⁵³ S. Polesya, S. Mankovsky, D. Benea, H. Ebert, and W. Bensch, *J. Phys.: Condens. Matter* **22**, 156002 (2010).
 - ⁵⁴ F. Ahmadian, M. R. Abolhassani, S. J. Hashemifar, and M. Elahi, *J. Magn. Magn. Mater.* **322**, 1004 (2010).
 - ⁵⁵ H. Nakayama, T. Fujita, and H. Raebiger, *Appl. Phys. Express* **6**, 073006 (2013).

- ⁵⁶ K. Momma and F. Izumi, J. Appl. Cryst. **44**, 1272 (2011).
- ⁵⁷ N. Papanikolaou, R. Zeller, and P. H. Dederichs, J. Phys.: Condens. Matter **14**, 2799 (2002).
- ⁵⁸ N. Stefanou, H. Akai, and R. Zeller, Comput. Phys. Commun. **60**, 231 (1990).
- ⁵⁹ N. Stefanou and R. Zeller, J. Phys.: Condens. Matter **3**, 7599 (1991).
- ⁶⁰ H. Ebert and R. Zeller, *The SPR-TB-KKR package*, URL: olymp.cup.uni-muenchen.de/ak/ebert/SPR-TB-KKR, also see kkrgf.org.
- ⁶¹ S. H. Vosko, L. Wilk, and M. Nusair, Can. J. Phys. **58**, 1200 (1980).
- ⁶² K. Wildberger, P. Lang, R. Zeller, and P. H. Dederichs, Phys. Rev. B **52**, 11502 (1995).
- ⁶³ A. I. Liechtenstein, M. I. Katsnelson, V. P. Antropov, and V. A. Gubanov, J. Magn. Magn. Mater. **67**, 65 (1987).
- ⁶⁴ N. Metropolis, A. W. Rosenbluth, M. N. Rosenbluth, A. H. Teller, and E. Teller, The J. Chem. Phys. **21**, 1087 (1953).
- ⁶⁵ M. Matsumoto and T. Nishimura, ACM Trans. Model. Comput. Simul. **8**, 3 (1998).
- ⁶⁶ V. P. Antropov, M. I. Katsnelson, B. N. Harmon, M. van Schilfgaarde, and D. Kusnezov, Phys. Rev. B **54**, 1019 (1996).
- ⁶⁷ S. V. Halilov, H. Eschrig, A. Y. Perlov, and P. M. Oppeneer, Phys. Rev. B **58**, 293 (1998).
- ⁶⁸ H. U. Baranger and A. D. Stone, Phys. Rev. B **40**, 8169 (1989).
- ⁶⁹ D. Bauer, *PhD Thesis, RWTH Aachen University* (2013).
- ⁷⁰ The resistivity measurements in Ref. 41 were reported up to 400 K, which was already above the Curie temperature.